# Analytic estimation of 3D noise power spectra in robot CBCT with arbitrary scan trajectories

Seungjun Yoo<sup>a</sup>, Seokwon Oh<sup>a</sup>, Junho Lee<sup>a</sup>, Seongbon Park<sup>a</sup>, Junwoo Kim<sup>b</sup>, and Ho Kyung Kim<sup>a,\*</sup>

<sup>a</sup> Computational X-ray Imaging Laboratory, School of Mechanical Engineering, Pusan Nat'l Univ., Busandaehakro
63beon-gil, Busan 46241

<sup>b</sup> Imaging R&D Lab, SAMSUNG MEDISON Co., Ltd., 1077, Cheonho-daero, Gangdong-gu, Seoul, 05340

\*Corresponding author: hokyung@pusan.ac.kr

## \*Keywords: Noise-power spectrum, Cascaded-system analysis, Robotic arm, Computed tomography

#### 1. Introduction

Signal, noise, and their spatial correlations fundamentally determine image quality and can be described using Fourier metrics such as the modulation-transfer function (MTF) and noise power spectrum (NPS). Their ratio defines noise-equivalent quanta (NEQ) or detective quantum efficiency (DQE), widely used to evaluate imaging performance. The cascaded-systems analysis (CSA) framework parameterizes signal and noise in terms of system properties (e.g., photon fluence, quantum efficiency, electronic noise, pixel fill factor), enabling identification of factors that degrade performance and guiding optimization [1].

CSA has been extended from 2D radiography to 3D cone-beam CT (CBCT), where additional filtering and backprojection introduce deterministic but irreversible effects due to sampling, making acquisition and reconstruction parameters critical determinants of image quality. Previous 3D CSA models propagated projection noise through the reconstruction pipeline, enabling computation of 3D NPS, NEQ, and DQE, and revealing trade-offs among dose, number of projections, filtering, binning, and noise aliasing [2]. Applications to breast tomosynthesis further highlighted the role of reconstruction filters in shaping image quality.

However, most analyses have assumed regular circular or limited-angle trajectories. With the advent of robotic CT systems [3], arbitrary and adaptive scan paths

tailored to object geometry are now feasible, offering flexibility but also introducing complex noise propagation not captured in conventional models. In this study, we extend the 3D CSA framework to CBCT with robotic arms, analyzing the effect of arbitrary scan trajectories on noise characteristics. The developed model is validated against measurements and provides a basis for optimizing scan paths in robot-assisted CT.

#### 2. Materials and methods

#### 2.1. 2D-to-3D CSA model for an arbitrary scan path

We have previously employed the 2D CSA model to investigate signal and noise transfer in X-ray detectors under a variety of configurations [4]. Here, we provide a brief overview of that model as a basis for extending the analysis to 3D CSA model. In this study, we assume a indirect X-ray detector model, as illustrated in fig. 1 (upper pipeline). The 2D CSA model comprises the following sequential stages: 0) incident X-ray quanta  $\tilde{q}_0$ , 1) quantum absorption efficiency  $\alpha$ , 2) quantum amplification m, 3) random relocation T, 4) coupling efficiency  $\eta$ , 5) aperture integration, 6) 2D sampling, 7) additive electronic noise  $\sigma_{\rm add}^2$ . Stages 1,2, and 4 correspond to gain processes, while stage 3 represents stochastic spreading (e.g., optical photon spread in X-ray converter), and stage 5 corresponds to deterministic

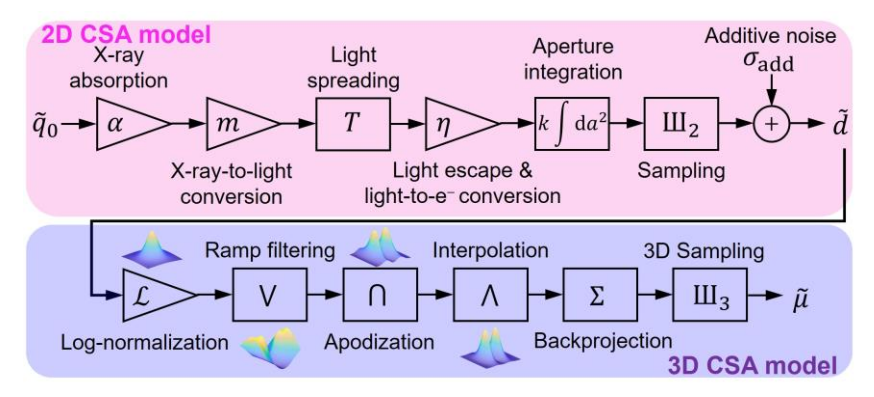


Figure. 1. Cascaded model describing noise propagation in an X-ray imaging detector and CT imaging. The upper pipeline illustrates the 2D CSA model, which describes the conversion of incident X-ray quanta into digital signal. The lower pipeline represents the 2D-to-3D CSA model, incorporating CT operations such as log-normalization, ramp filtering, apodization, interpolation, and backprojection, followed by 3D sampling.

spreading due to the sinc function. The resulting NPS at the detector output can be expressed as:

$$W(\mathbf{u}) = \sum_{\mathbf{i}} \frac{d^2}{\bar{q}_0} \left[ \frac{1}{G} + \frac{1}{\alpha} \left( \frac{1}{I_m} - \frac{1}{m} \right) T^2 \operatorname{sinc}^2(a\mathbf{u}) \right] \delta\left(\mathbf{u} - \frac{\mathbf{i}}{p}\right) + \sigma_{add}^2.$$
 (1)

The overall system gain is given by  $G = ka^2 \alpha m\eta$ , where, k is the conversion gain [ADU/ $e^-$ ], and a is the aperture size. In this model, the spatial frequency vector is defined as  $\mathbf{u} = (u, v, w)^T$ , corresponding to the 2D frequency components in the detector plane. The pixel index and pixel pitch are denoted as  $\mathbf{i} = (i, j)^T$  and p. The aperture function is assumed to be rectangular with width a, and the corresponding transfer function in the frequency domain is expressed as  $\operatorname{sinc}(a\mathbf{u}) = \operatorname{sinc}(a\mathbf{u}) \operatorname{sinc}(a\mathbf{v})$ .

To extend the 2D CSA to a 3D CSA model, a minimum of six additional stages must be incorporated into the imaging chain, as summarized in fig. 1 (lower pipeline). Before reconstruction, detector signals are converted to attenuation images through logarithmic normalization, yielding " $\mu$ t image" that represent pathintegrated attenuation. Following Tward et al. [2], the effect of this normalization on the NPS can be approximated by a division by the squared mean detector signal  $\tilde{d}^2$  and is given

$$W'(\mathbf{u}) = W(\mathbf{u})/\tilde{d}^2. \tag{2}$$

After logarithmic normalization, the imaging chain proceeds through three deterministic spreading stages: ramp filtering, apodization filtering, and interpolation. Ramp filtering compensates for system blur but amplifies high-frequency noise, which is mitigated by apodization filters (e.g., Shepp–Logan, cosine, Hamming, or Hann); in this study, a Hann window was used. Interpolation, required because backprojection values rarely align with detector pixel centers, introduces deterministic smoothing characterized in the frequency domain by a squared sinc function (for bilinear interpolation). Collectively, these processes affect the NPS multiplicatively and are modeled by the product of the squared transfer functions:

$$W^*(\mathbf{u}) = W'(\mathbf{u})T_V^2 T_0^2 T_\Lambda^2. \tag{3}$$

The filtered projections are subsequently backprojected into image space, and according to the Fourier slice theorem, each projection maps to a specific region in the frequency domain depending on the scan angle. In the case of a conventional circular trajectory, the acquired data are populated in the frequency domain in a cylindrical manner. However, to account for arbitrary scan paths, an additional coordinate transformation is required. We employ the ZYZ extrinsic rotation matrix to represent arbitrary source orientations and appropriately map their contributions in the

frequency domain. To project the detector frequency components into the 3D spatial frequency domain, we define two orthonormal vectors  $\mathbf{v}_i$  and  $\mathbf{w}_i$  for each projection angle i, which describe the mapping directions of the detector's horizontal and vertical frequency axes, respectively. These vectors are derived from parameterized angles  $(\alpha_i, \beta_i, \gamma_i)$ , corresponding to rotations about z-, y-, and z- axes. Specifically, the directional vector  $\mathbf{v}_i$  corresponding to the detector u- axis is given by:

$$\mathbf{v}_{i} = \begin{bmatrix} -\cos\gamma_{i}\cos\beta_{i}\sin\alpha_{i} - \sin\gamma_{i}\cos\alpha_{i} \\ -\sin\gamma_{i}\cos\beta_{i}\sin\alpha_{i} + \cos\gamma_{i}\cos\alpha_{i} \\ \sin\beta_{i}\sin\alpha_{i} \end{bmatrix}, \tag{4}$$

And the vector  $\mathbf{w}_i$  corresponding to the detector v – axis is:

$$\mathbf{w}_{i} = \begin{bmatrix} \cos \gamma_{i} \sin \beta_{i} \\ \sin \gamma_{i} \sin \beta_{i} \\ \cos \beta_{i} \end{bmatrix}. \tag{5}$$

These vectors enable the transformation of 2D detector frequency components into the appropriate 3D spatial frequency locations in the reconstructed volume. This formulation ensures modeling of the noise propagation behavior under arbitrary scan trajectories. Consequently, the backprojected 3D NPS is given by:

$$\widehat{W}(\mathbf{f}) = \frac{1}{\Delta f} \left(\frac{2\pi M}{m\omega}\right)^2 W^*(f_u, f_v) \sum_{i=1}^m \delta(f - f_u \mathbf{v}_i - f_v \mathbf{w}_i).$$
(6)

Where  $f = (f_x, f_y, f_z)^T$  is the spatial frequency vector in the 3D image domain, and  $(f_u, f_v) = (\frac{u}{M}, \frac{v}{M})$  are the detector frequency components scaled by magnification factor M. The parameter  $\omega$  represents the redundancy factor, and m is the number of projectionss. The term  $\Delta f = \frac{M}{2pN_{\rm bin}}$  denotes the frequency sampling interval, with  $N_{bin}$  representing the number of discrete frequency samples up to the Nyquist frequency used in the model. Finally, by applying 3D sampling based on the reconstructed voxel size, NPS for the arbitrary scan paths can be obtained

$$W(\mathbf{f}) = \sum_{\mathbf{j}} \widehat{W}(\mathbf{f}) \delta\left(\mathbf{f} - \frac{M}{n}\mathbf{j}\right). \tag{7}$$

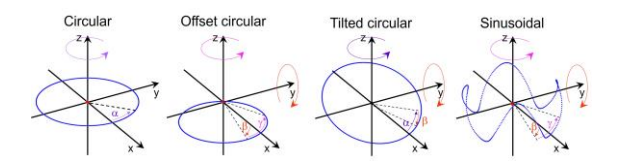


Figure. 2. Scan paths defined for analyzing the noise properties: circular, offset circular, tilted circular, and sinusoidal.

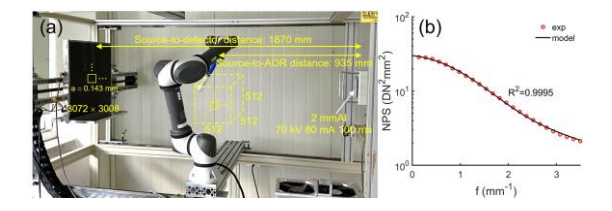


Figure. 3. (a) Robot CT system for arbitrary scanning. The system integrates a robotic arm into a conventional X-ray imaging configuration, enabling flexible object manipulation during data acquisition. (b) NPS of the 2D detector, with experimental data (red circles) closely fitted by a least-squares regression model (black line).

Where  $\mathbf{j} = (i, j, k)^T$  is denoted as voxel index.

# 2.2. Trajectory configuration

Using the extrinsic ZYZ angles in the model, the scanning trajectory was constructed by specifying a sequence of source poses relative to the global coordinate system. This approach allows for flexible description of arbitrary 3D scan paths in robot CT. As shown in fig. 3, four types of scanning trajectories were configured. In all cases, the X-ray source was oriented to continuously face the origin (object center), while the detector was positioned on the line connecting the source center and the origin, located on the opposite side of the object.

The circular trajectory corresponds to the conventional CBCT trajectory. The offset circular trajectory can be expressed as  $\{\Omega:\alpha=0,\beta=\pi/6,\gamma\in[0,2\pi]\}$ . The tilted circular trajectory is described as  $\{\Omega:\alpha\in[0,2\pi],\beta=\pi/6,\gamma=0\}$ . The sinusoidal trajectory, where the source moves along the sine curve, is described as  $\{\Omega:\alpha=0,\beta=(\pi/6)\text{sin}4\gamma,\gamma\in[0,2\pi]\}$ . In addition, we analyzed fully arbitrary trajectories based on our current study, where scan trajectories are designed to reduce metal artifacts.

## 2.3. Experimental setup

To validate the proposed model, experiments were conducted using a robot CT system built in our laboratory. As shown in fig. 3, the system integrates a robotic arm into a conventional radiographic imaging setup, allowing object manipulation during scanning. In this study, however, only flood-field imaging for the NPS measurement was performed without additional robotic control. The X-ray imaging system consisted of a tungsten-target X-ray tube (E7239X, Toshiba Co., Japan) and a generator (DRGEM Co., Ltd., Korea). The exposure conditions were set to 70 kV, 80 mA, and 100 ms with a 2-mm aluminum filtration. The detector used was an amorphous silicon (a-Si:H) TFT-based flat-panel detector (FDX4343R, Toshiba Co., Japan), equipped with a 0.5-mm-thick CsI:Tl scintillator. The detector features a format of 3008 × 3072 pixels with a pixel pitch of 0.143 mm. A total of 380 flood-field images and 20 dark-field images were acquired. Among them, 20 images were used for 2D NPS measurements, while the remaining flood-field images were used for 3D NPS analysis.

3D image reconstruction was performed using the Feldkamp–Davis–Kress algorithm. The reconstructed volume consisted of  $512 \times 512 \times 512$  voxels with an isotropic voxel size of p/M = 0.0715 mm. A Hann apodization filter was applied during reconstruction, with the cutoff frequency set to the Nyquist frequency.

The 2D NPS measurement was performed in accordance with IEC recommendations [5], using ensemble averaging over 160 regions of interest of size 256 × 256 pixels. This work focuses on validating the 3D CSA model, for which the measured 2D NPS was fitted using a least-squares regression with a function consisting of a Gaussian and an exponential term, and the fitted result, as shown in fig. 3(b), was applied to eq. 1. The 3D NPS was calculated from the extracted volume of interests (VOIs) using the following equation:

$$NPS(\mathbf{f}) = \frac{(p/M)^3}{L^3} \langle |DFT\{\Delta I(\mathbf{x})\}|^2 \rangle.$$
 (8)

Where L = 128 denotes the side length of the VOI, and  $\mathbf{x} = (x, y, z)^T$  represents the spatial position vector of volume date. The term  $\Delta I(\mathbf{x})$  refers to the zero-mean volume obtained by subtracting the mean of the reconstructed image. A total of 45 VOIs were extracted for ensemble averaging. Specifically, 15 VOIs were

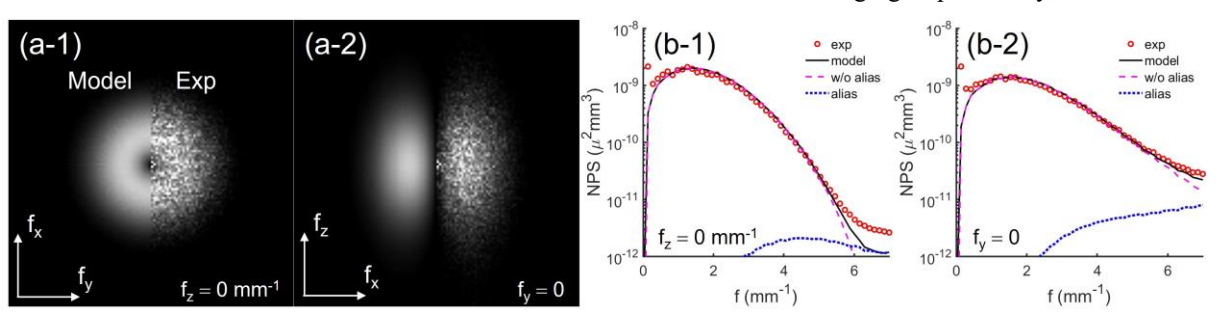


Figure. 4. Comparison between model-predicted and measurement for the circular trajectory. (a-1, a-2) Slices of the 3D NPS at  $f_z = 0 \text{ mm}^{-1}$  and  $f_y = 0 \text{ mm}^{-1}$ , respectively. The left half of each image shows the model prediction, and the right half shows the experimental result. (b-1, b-2) Radially averaged profiles of (a-1) and (a-2), respectively. The model (black line), experimental data (red circles), model without aliasing (magenta dashed line), only aliasing are shown.

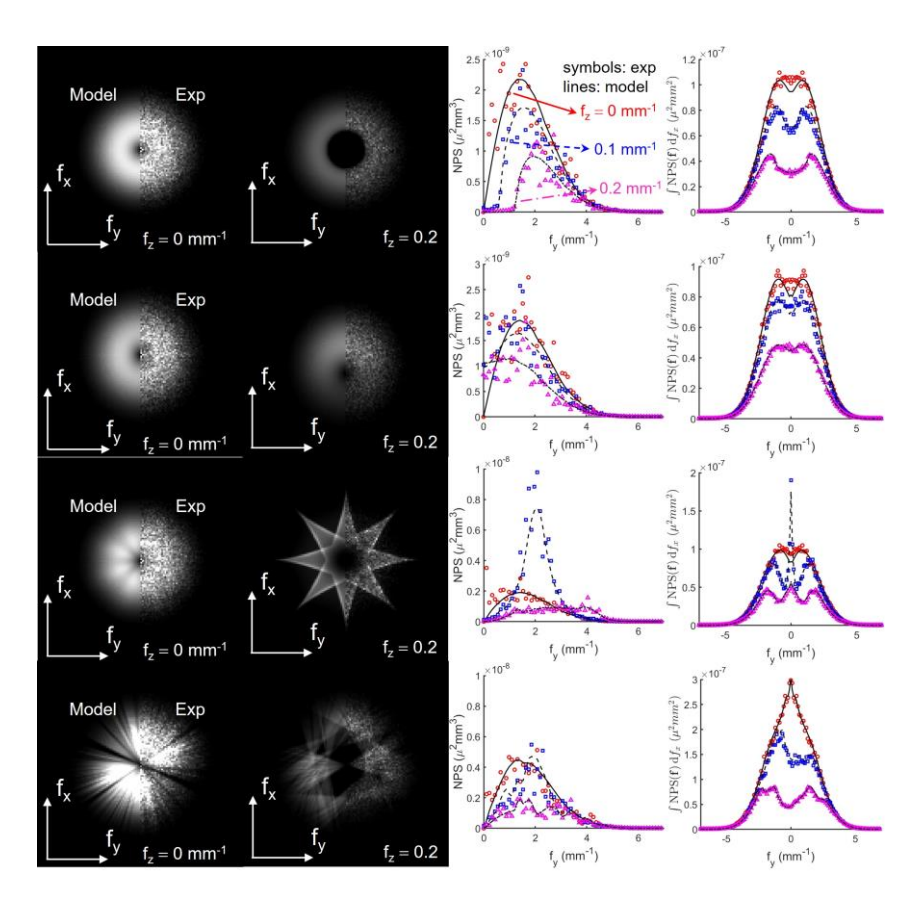


Figure. 5. Comparison of model-predicted and experimentally measured 3D NPS under four different scan paths: offset circular, tilted circular, sinusoidal, and arbitrary, from top to bottom. The first and second columns show 2D NPS slices at  $f_z = 0 \text{ mm}^{-1}$  and  $f_z = 0.2 \text{ mm}^{-1}$ , respectively. The third column presents 1D NPS profiles along  $f_y$  at  $f_z = 0$ , 0.1, and 0.2 mm<sup>-1</sup>, extracted at  $f_x = 0 \text{ mm}^{-1}$ . Experimental data are shown as symbols and model predictions as lines. The fourth column shows the NPS integrated along the  $f_x$  direction.

selected from slices near the central axial plane, while the remaining 30 VOIs were taken from slices located approximately 100 voxels above and below the center, with 15 VOIs from each.

## 3. Results

#### 3.1. Validation

Fig. 4 compares the model-predicted 3D NPS with the experimentally measured 3D NPS. fig. 4(a-1) and (a-2) show 2D slices of the 3D NPS at  $f_z = 0 \ mm^{-1}$  and  $f_y = 0 \ mm^{-1}$ , respectively. In both images, the left half represents the model prediction, and the right half shows the experimental results. All images are displayed using the same window level range of  $\pm 3\sigma$  for consistent visual comparison. The corresponding radially averaged profiles of the slices are plotted in fig. 4(b-1) and (b-2). The model without aliasing corresponding to eq. 6, and the aliasing was derived by subtracting eq. 6 from eq. 7. While some discrepancies were present, particularly at zero and high spatial frequencies, the model demonstrated a capability to replicate the overall characteristics of the experimental NPS.

# 3.2. NPS analysis for various scan trajectories

Fig. 5 shows how different scan paths influence the 3D NPS in terms of shape and frequency characteristics. Although the conventional CBCT CSA model modified for the arbitrary scan path, it still accounts well for the measured NPS, as observed in fig. 6. In the offset circular trajectory, the NPS exhibits a nearly isotropic shape at the transaxial slices. Its shape is similar to that of the circular trajectory and appears toroidal, but the central null space becomes larger as the slice moves farther from the central plane. This indicates that, as the spatial frequency moves away from zero along the  $f_z$  direction, a larger portion of low-frequency components in the  $f_x$ and  $f_v$  directions is lost. The 3D NPS for the tilted circular scan path is a version of the tilted 3D circular NPS. The sinusoidal trajectory introduces periodic variations in the frequency components, as seen in the star-shaped patterns in the higher  $f_z$  slice. Under the arbitrary scan path, the NPS becomes highly irregular and strongly anisotropic, with distinct directional components and nonuniform frequency distribution.

# 4. Discussions and future studies

We extended the conventional 3D CSA model for NPS characterization in CBCT by modifying the backprojection operation to accommodate arbitrary scan trajectories. Experimental validation across multiple trajectories confirmed that the model predictions were in reasonable agreement with the measurements. Some discrepancies between the model predictions and experimental results near zero frequency are likely attributable to long-range nonuniformities in the measurements, which may have arisen from an incomplete detrending procedure. A more detailed analysis will be presented at the conference.

In further work, the proposed model will provide a theoretical foundation to optimize scan trajectories in robot CT systems by assessing task-specific imaging performance, with particular attention to the influence of noise patterns on detectability.

## **REFERENCES**

This work was supported by the National Research Foundation of Korea (NRF) grant funded by the Korea government (MSIT) (RS-2024-00340520).

#### REFERENCES

- [1] H. K. Kim, Development of energy-integrating detectors for large-area X-ray imaging, in Radiation detection systems (K. Iniewski and J. S. Iwanczyk, eds), Ch. 7, CRC Press, Boca Raton, 2021.
- [2] D. J. Tward, and J. H. Siewerdsen, Cascaded systems analysis of the 3D noise transfer characteristics of flat-panel cone-beam CT, Medical Physics, Vol. 35, No. 12, pp. 5510-5529, 2008.
- [3] W. Holub, F. Brunner, and T. Schön, RoboCT application for in-situ inspection of join technologies of large scale objects, International Symposium on Digital Industrial Radiology and Computed Tomography, 2019.
- [4] S. Yoo, S. Park, S. Yun, and H. K. Kim, Impact of the fiber-optic faceplate on the imaging performance of a CMOS X-ray detector, Journal of Instrumentation, Vol. 19, No. 12, P12003, 2024
- [5] IEC, Medical electrical equipment Characteristics of digital X-ray imaging devices—Part 1-1: Determination of the detective quantum efficiency—Detectors used in radiographic imaging, Tech. Rep. 62220-1-1, International Electrotechnical Commission, 2015.